Natural convection of water in a rectangular cavity including density inversion

Wei Tong* **and Jean N. Koster**
Department of Aerospace Engineering Sciences, University of Colorado, Boulder, CO, USA

Two-dimensional natural convection in water with density inversion is studied numerically in a rectangular cavity. The non-Boussinesq parabolic density-temperature relationship is incorporated in a finite element model. Numerical results are obtained for Rayleigh numbers up to 10^6. The evolution of the temperature field and flow pattern show that density inversion and initial location of the maximum density surface within the liquid have a determining effect on convection character. The investigation of aspect ratio on flow character is also presented. It is found that interactive convection across the density inversion surface is dependent on aspect ratio and Rayleigh number.

Keywords: natural convection; non-Boussinesq fluids; density inversion

Introduction

In studies of buoyancy-induced flows, Boussinesq approximation is commonly used to simplify flow models. This approximation consists of two parts: (1) varying thermophysical properties are neglected in the governing equations for density in the momentum equation for the vertical direction. (2) The density is a linear function of temperature. Conditions are non-Boussinesq if one of these conditions is violated. It is known that some fluids exhibit density inversion behavior in specific temperature ranges. Close to these density maxima the density changes in a nonlinear parabolic fashion. These systems develop convective flow for any direction of the temperature gradient. A common example is water which possesses a maximum density of 3.98°C under standard conditions. Other examples are liquid helium, which has a density inversion at about 2.18 K (Walden and Ahlers, 1981), and the pseudobinary electronic alloy $Hg_{1-x}Cd_xTe$ with an inversion at 1,028 K (Chandra and Holland 1983).

The studies of density inversion have been associated with two topics: (1) Rayleigh-Bénard instability and (2) natural convection. In the first class of problems a fluid is subjected to vertical temperature gradients. At a critical Rayleigh number, convection (often referred to as "penetrative convection") develops in the unstable lower layer and extends into the stable upper layer (e.g., Merker et al. 1973; Moore and Weiss 1973; Musman 1968; Robillard and Vasseur 1981; Veronis, 1963). In the second class, a fluid is contained within an enclosure where two adjacent vertical walls are at different temperature. Natural convection is thus generated at the cold and hot vertical walls. This study concentrates on the second class of problems.

Watson (1972) analyzed the effect of density inversion on the fluid flow and heat transfer in a square vessel. In his study, the Rayleigh number was restricted to $Ra \leq 2 \times 10^4$. The results showed that the inversion effect is maximized when $\Delta T = 8$°C. The effect of temperature-dependent viscosity was also investigated. It was found that though the fluid viscosity can change by 20 percent at the temperature range of 0–8°C, the influence of variable viscosity on the flow character is rather small. Seki et al. (1978) investigated natural convection both numerically and experimentally in rectangular vessels. The cold vertical wall was maintained at 0°C, and the hot wall temperature was varied from 1–12°C. Their experimental and numerical results of flow pattern and temperature distribution were found to be in good agreement for $\Delta T \leq 8$°C and $A = 5$, and in fair agreement for $\Delta T = 10$°C. More recently, Lin and Nansteel (1987) investigated natural convection in a square enclosure containing water near its density maximum. In their study the multicellular flow structures were observed for certain ranges of the density distribution parameter, which is independent of the value of Rayleigh number.

The present work expands on the previous studies of natural convection in water with density inversion confined to a rectangular two-dimensional (2-D) cavity. By setting the temperature of the left wall to 0°C and varying the temperature at the right wall higher than 3.98°C, the vertical plane of the maximum density surface occurs inside the liquid volume. A parabolic density profile is incorporated in the finite element model. Two vertically separated liquid layers are created: the left layer with a positive density gradient in horizontal direction, and the right-side layer with a negative density gradient. Natural convection rolls of opposite vorticity develop in both layers, when for linear density profile only one roll develops. With a parabolic density correlation the governing equations become highly nonlinear. The case studies range from Rayleigh numbers 10^3–10^6.

Mathematical formulation

The configuration of interest is illustrated in Figure 1. A rectangular cavity of aspect ratio $A = H/L$ is filled with water and differentially heated from two vertical sides. The top and bottom surfaces are adiabatic. The flow is assumed to be

Address reprint requests to Professor Koster at the Department of Aerospace Engineering Sciences, University of Colorado, Boulder, CO 80309, USA.
* Current address: Rensselaer Polytechnic Institute, Department of Mechanical Engineering, Troy, NY 12180-3590, USA

Received 16 December 1992; accepted 29 June 1993

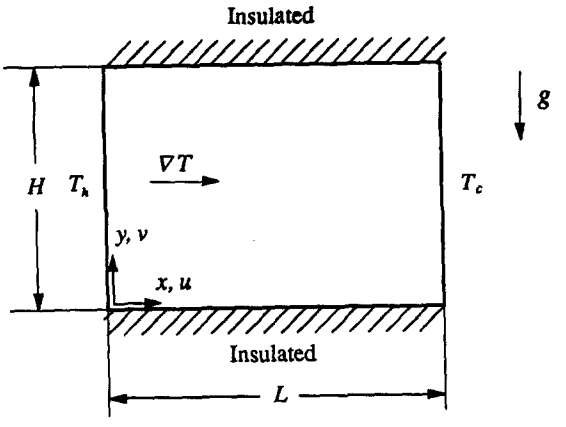

Figure 1 Schematic of the flow configuration

laminar, steady, incompressible, and 2-D. The parabolic density-temperature relationship is given as

$$\frac{\rho}{\rho_o} = 1.0 - \gamma(T - T_0)^2 \tag{1}$$

where $\gamma = 8.0 \times 10^{-6}$ $(°C)^{-2}$ and ρ_0 is the maximum density at the temperature $T_0 = 3.98°C$. This correlation has been widely used in studies of density inversion problems (Moore and Weiss 1973; Musman 1968; Tien 1968). Though there are several models to cover wider temperature ranges for the density-temperature behavior (e.g., Gebhart and Mollendorf 1978; Sun et al., 1969), the relative difference between these models is found negligibly small (<0.01%) for the temperature range of 0–12°C.

Two case studies were performed. The first case excludes density inversion, and the maximum density coincides with the hot wall ($T_h = 3.98°C$). These calculations provide detailed information on the evolution of the temperature field and convective roll cell pattern with increasing Rayleigh number. The second case includes density inversion within the bulk of the liquid by maintaining $T_c = 0°C$ and varying T_h ($3.98°C < T_h \leq 12°C$). This condition positions the maximum density plane within the liquid. Two regions develop with two counter-rotating rolls of opposite vorticity.

The governing equations, expressing conservation of mass, momentum, and energy, based on the assumption of constant fluid properties except for the density in the body force term, are nondimensionalized using the following variables:

$$X = \frac{x}{L}; Y = \frac{y}{L}$$

$$\mathbf{U} = \frac{\mathbf{u}}{\frac{\alpha}{L}\sqrt{\mathrm{Ra\ Pr}}}; \theta = \frac{T - T_0}{\Delta T} \tag{2}$$

$$P = \frac{p}{\frac{\mu\alpha}{L^2}\sqrt{\mathrm{Ra\ Pr}}}$$

where $\Delta T = T_h - T_c$, $\mathbf{U} = \{U, V\}$ the velocity vector. The Rayleigh and Prandtl number are defined as

$$\mathrm{Ra} = \frac{g\gamma(\Delta T)^2 L^3}{\alpha\nu} \tag{3}$$

$$\mathrm{Pr} = \frac{\nu}{\alpha} \tag{4}$$

Note that the Rayleigh number is based on the horizontal temperature difference $(\Delta T)^2$ and $\gamma(^0C^{-2})$, rather than ΔT and β $(°C^{-1})$ as in traditional cases. In this study, the Prandtl number is calculated at $T = 3.98°C$ and therefore fixed at Pr = 11.57. Thus, for a fixed temperature difference, the Rayleigh number is varied by modifying the cavity width, L. It has been reported (FIDAP, 1990) that the preceding setting is most advantageous in numerical simulations for strongly coupled flows.

The resulting steady-state dimensionless equations are expressed as

$$\nabla \cdot \mathbf{U} = 0 \tag{5}$$

$$\sqrt{\frac{\mathrm{Ra}}{\mathrm{Pr}}}(\mathbf{U} \cdot \nabla \mathbf{U}) = -\nabla P + \nabla^2 \mathbf{U} - \sqrt{\frac{\mathrm{Ra}}{\mathrm{Pr}}}\theta^2 \mathbf{e} \tag{6}$$

$$\sqrt{\mathrm{Ra\ Pr}}(\mathbf{U} \cdot \nabla\theta) = \nabla^2\theta \tag{7}$$

where $\mathbf{e}$ is the vertical unit vector in the negative Y-coordinate. From Equation 6, it can be seen that the buoyancy effect is characterized by the ratio Ra/Pr, i.e., the Grashof number.

Notation

A	Aspect ratio, $A = H/L$
g	Gravitational acceleration
h	Heat-transfer coefficient
H	Cavity height
k	Thermal conductivity
L	Cavity width
Nu	Nusselt number
p	Pressure
P	Dimensionless pressure
Pr	Prandtl number
Ra	Rayleigh number
T	Temperature
T_0	Temperature at maximum density ρ_0
ΔT	Temperature difference, $T_h - T_c$
$\mathbf{u}$	Velocity vector, $\mathbf{u} = \{u, v\}$
$\mathbf{U}$	Dimensionless velocity vector, $\mathbf{U} = \{U, V\}$
U, V	Dimensionless velocities in x and y coordinates
x, y	Coordinates
X, Y	Dimensionless coordinates

Greek symbols

α	Thermal diffusivity
θ	Dimensionless temperature
μ	Dynamic viscosity
ν	Kinematic viscosity
ρ	Density
ρ_0	Maximum density
ψ	Stream function
Ψ	Dimensionless stream function

Subscripts

c	Cold
h	Hot
l	Liquid

The governing Equations 5–7 are subjected to no-slip boundary conditions at all solid walls, and constant temperature and adiabatic conditions apply, respectively, at vertical and horizontal walls:

$$\mathbf{U} = 0; \theta = \theta_h \text{ at } X = 0$$

$$\mathbf{U} = 0; \theta = \theta_c \text{ at } X = 1 \tag{8}$$

$$\mathbf{U} = 0; \frac{\partial \theta}{\partial Y} = 0 \text{ at } Y = 0, A$$

It is to be noted that the position of the top boundary is based on the aspect ratio. Initially the aspect ratio is set to 1.0. The effect of aspect ratio on the temperature and convective fields will be addressed separately.

Numerical solution procedure

The nonlinear governing Equations 5–7 were discretized using a finite-element procedure (FIDAP, 1990). The code FIDAP is based on the Galerkin formulation.

One contribution of this article is the description of the parabolic density profile (Equation 1) with FIDAP. Nonuniform nine-node quadrilateral elements were employed for the discretization of temperature and velocity. To obtain accurate results for the sharply varying flow variables in near-wall regions, a fine staggered mesh was used.

To study the effect of the grid size on the solutions, a series of calculations were performed by varying the number of grid points in each direction. The results of the grid point independence study are given in Table 1. For $A = 1$, it was found that at $\text{Ra} = 5 \times 10^4$ the average Nusselt number changes less than 0.05 percent as the grid point varies from 43×43 (21×21 element meshes) to 55×55 (27×27 element meshes). At $\text{Ra} = 10^5$ the change is still less than 0.09 percent. Therefore, 43×43 grid points are considered optimal for this study. For the cases $A \neq 1$, the grid point was adjusted according to A values. Table 5 lists the optimal number of grid points employed for different values of A.

Convergence of the numerical calculations is achieved whenever the following criteria are satisfied:

$$\frac{\|\mathbf{u}_i - \mathbf{u}_{i-1}\|}{\|\mathbf{u}_{i-1}\|} \leq 10^{-4} \tag{9}$$

$$\frac{\|R(\mathbf{u}_i)\|}{\|R_o\|} \leq 10^{-4} \tag{10}$$

where $\|\cdot\|$ is the Euclidean norm and $\mathbf{u}_i$ is the solution vector and $R(\mathbf{u}_i)$ is the residual vector (i indicates the ith iteration). Because both $\Delta\mathbf{u}_i$ and $R(\mathbf{u})$ tend to zero near the real solution, a combination of these two criteria provides a sufficient and effective overall convergence criterion for all possible situations.

Nonlinear solutions were obtained by using the combination of two iterative methods, Successive Substitution (SS) and Newton-Raphson (NR). The solution procedure used in this analysis was to start at each Rayleigh number (taken as the loading parameter) with 2 or 3 iterations of the SS method followed by 5 to 40 additional iterations of the NR method. The strategy of using the slower but more robust SS-method in the early phase of the calculations was to bring the solution within the radius of convergence of the faster converging NR method.

It was found that in some cases obtaining converged solutions becomes very difficult. This difficulty results from the application of the conventional Galerkin finite element method, which uses centered differences in the convection term. This causes oscillatory behavior (wiggles) of velocity or any other flow variable (Sohn 1988). The common ways to eliminate wiggles are (1) by mesh refinement in the computational domain and (2) by applying a stream upwinding scheme (balancing tensor diffusivity type). In the present study, both methods are applied.

Table 1 Grid point independence study for $\Delta T = 12°C$

Grid	Ra	$\overline{\text{Nu}}$	Ra	$\overline{\text{Nu}}$
11×11	5×10^4	2.8062	10^5	3.5566
21×21		2.6916		3.3440
35×35		2.6744		3.3092
43×43		2.6722		3.3045
55×55		2.6709		3.3016

Table 2 Comparison of Nusselt number for $T_h = T_0$ (without density inversion)

Ra	Lin & Nansteel 21×21–41×41 —	de Vahl Davis 41×41 uniform	This Study 43×43 nonuniform
10^3	1.118	1.116	1.119
10^4	2.278	2.234	2.274
10^5	4.709	4.487	4.717
10^6	9.195	8.811	9.270

Results and discussion

Evolution of temperature field and convective flow pattern

The results of temperature and convective flow fields are presented in the form of isotherm and streamline contour plots. The dimensionless stream function, Ψ, is obtained from velocity field solutions by evaluating

$$\Psi = \int_0^A \mathbf{U}\, dY \tag{11}$$

along constant X-coordinate lines and $\Psi = \psi/[\alpha(\text{Ra Pr})^{1/2}]$.

To gain confidence in the algorithm, the simulation of natural convection is first performed without density inversion by setting $T_h = T_0$ (Figure 1). Thus, density becomes a monotonic (but still parabolic) function of temperature and $\partial\rho/\partial x < 0$. Then $T_h > T_0$ were studied to include a parabolic density profile. The computational results are compared with available solutions by Lin and Nansteel (1987) for convection including density inversion influence and those by de Vahl Davis (1983) for regular natural convection without density inversion. Though Lin and Nansteel (1987) employed a different density-temperature model than used in this study, the differences between both results are less than 0.9 percent for all Rayleigh numbers (Table 2). De Vahl Davis's solutions are referenced for two reasons: (1) This study considers a Prandtl number of 11.57 (for water), and de Vahl Davis considers $\text{Pr} = 0.73$ (for air). (2) This study uses a nonlinear density temperature correlation, and de Vahl Davis uses a linear correlation. The comparison between de Vahl Davis and this study demonstrates that the influence of small Prandtl number variations and nonlinear density functions become significant

Table 3 Numerical results at various Ra and ΔT in square cavities (A = 1) with 43 × 43 nodes

Ra	ΔT (°C)	$\overline{Nu}$	Ψ_{max} ($\times 10^3$)	$\lvert\Psi_{min}\rvert$ ($\times 10^3$)	U_{max}(@ node #)
10^3	3.98	1.119	11.032	0	0.039 (@ 1398)
	8.0	1.001	1.136	1.206	0.008 (@ 925)
	12.0	1.017	0.025	4.374	0.018 (@ 409)
10^4	3.98	2.274	15.318	0	0.064 (@ 1484)
	8.0	1.066	3.451	3.749	0.025 (@ 926)
	12.0	1.581	0.107	9.527	0.039 (@ 366)
10^5	3.98	4.717	10.474	0	0.073 (@ 1613)
	8.0	2.005	4.909	5.364	0.040 (@ 928)
	12.0	3.305	0.603	8.344	0.049 (@ 281)
10^6	3.98	9.270	6.071	0	0.075 (@ 1700)
	8.0	4.120	5.601	5.645	0.057 (@ 927)
	12.0	6.516	1.816	5.228	0.053 (@ 196)

Note: The node is counted from the left to the right and from the bottom to the top.

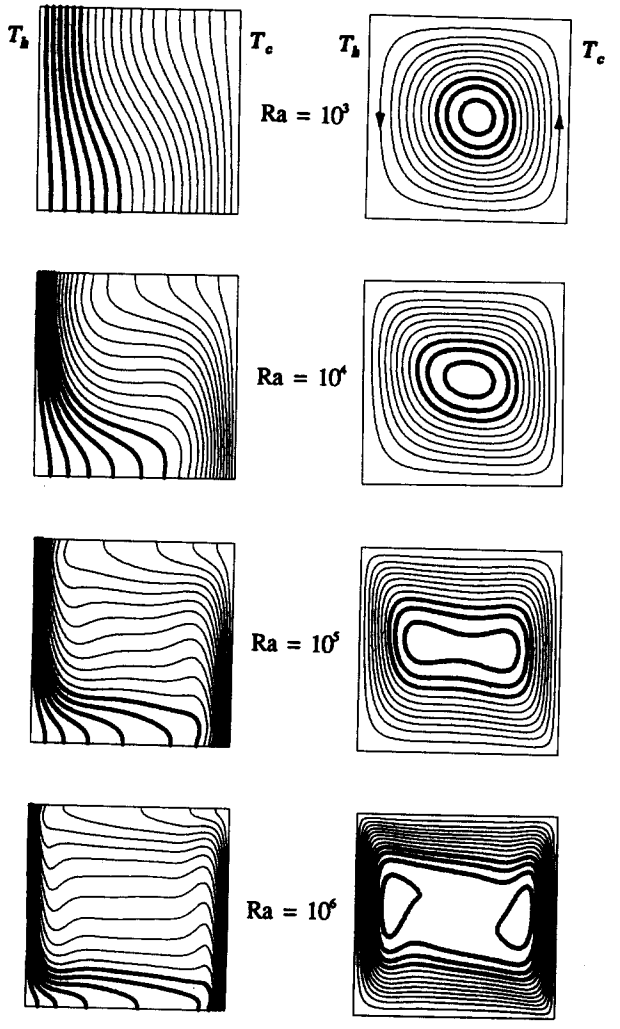

Figure 2 Evolution of the temperature field (left column) and convective flow pattern (right column) for ΔT = 3.98°C without density inversion. Dark lines represent the higher θ and Ψ values (FIDAP-plot routine feature)

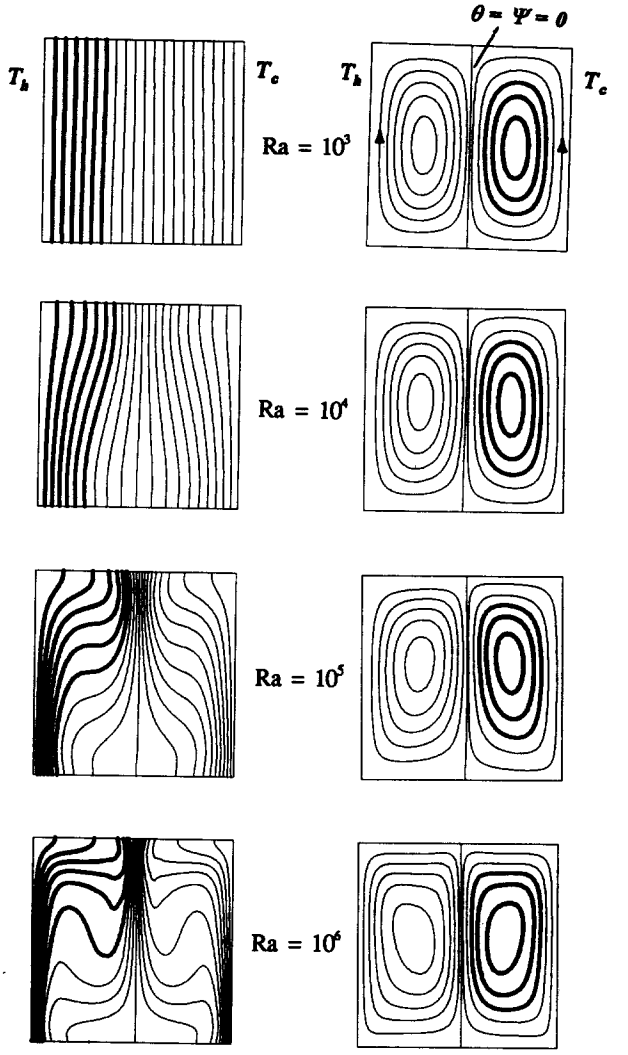

Figure 3 Evolution of the temperature field (left column) and convective flow pattern (right column) for ΔT = 8°C

only at large Rayleigh numbers (but still less than 5 percent in our study range).

The contours of stream function Ψ and temperature θ, for $\Delta T = 3.98$°C, are given in Figure 2 at various Rayleigh numbers. From this figure, unicellular flow is seen to be generated from the cold wall. As Ra increases the temperature gradients near the top of the left (hot) wall and the bottom of the right (cold) wall become large, and the convective roll cell in the cavity develops internal return flow (Ra = 10^5 and 10^6).

When ΔT is set to 8°C (i.e., $T_h = 8$°C), the maximum density surface is very close to the central vertical plane of the cavity. Convection starts as a counterrotating pair of roll cells separated by the density inversion plane (Figure 3). The vortex adjacent to the cold wall is moving counterclockwise with positive Ψ values. The density maximum surface separates the two roll cells; no penetration of one convection cell across the density inversion plane is observed. The density inversion plane acts like a liquid-liquid interface, although the liquids are totally miscible. Both layers behave like two immiscible liquid layers with perfect viscous and thermal coupling and without interfacial forces. In all cases, convective flow retains approximate symmetry with respect to the vertical centerline.

In the case of $\Delta T = T_h = 12$°C (Figure 4) the density inversion plane, which is included in the vorticity plot, is shifted

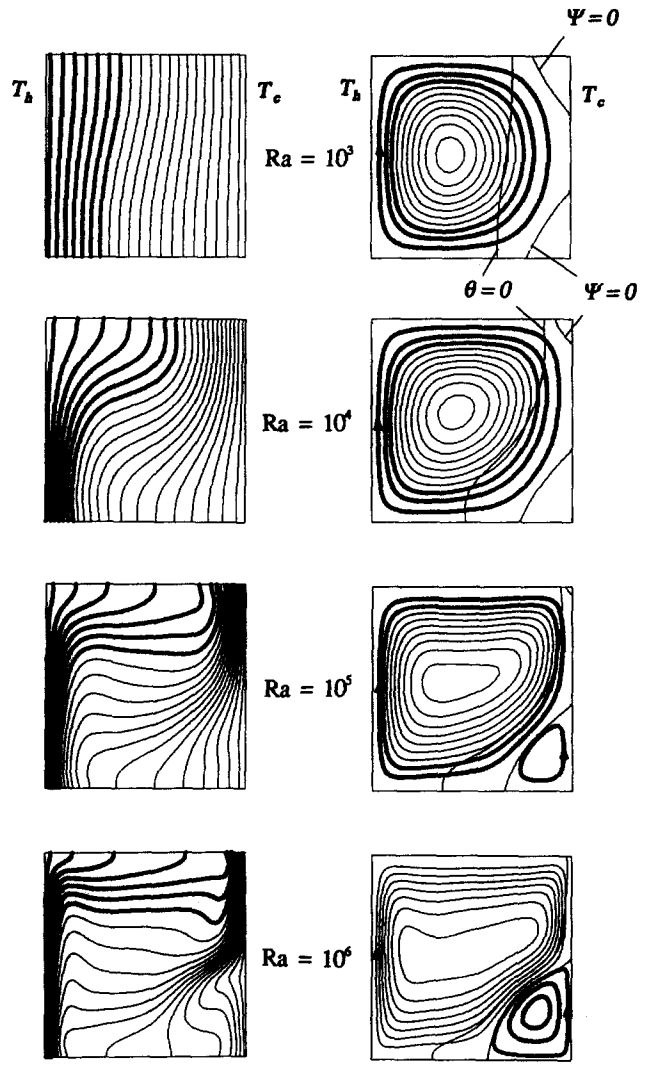

Figure 4 Evolution of the temperature field (left column) and convective flow pattern (right column) for ΔT = 12°C

toward the right cold wall. Single roll convection now penetrates across the density inversion plane as visualized in the flow patterns into which the $\theta = 0$ line is transposed. The right corner regions show no or extremely weak flow. This single roll cell pattern remains until much higher Rayleigh numbers are imposed. The density inversion plane, however, becomes deformed, and the no-flow region in the lower corner becomes larger, whereas the upper corner region becomes smaller. At sufficiently high Rayleigh number a small counterrotating second roll cell develops in the lower cold corner and acquires substantial strength at very high Ra. The roll fills up almost the whole region up to the density inversion plane. Within the limits of our calculations, however, the second roll remains much smaller than the first roll at the hot side of the cavity. The calculated results for various ΔT values are summarized in Table 3.

Table 4 C and m values in equation (17)

ΔT	C	m
3.98	0.160	0.294
8.0	0.078	0.283
12.0	0.111	0.294

Heat transfer at vertical walls

Local and average Nusselt number profiles play an important role in the analysis of heat transfer mechanism. The local heat-transfer rates at the horizontal rigid walls can be expressed in terms of the local Nusselt number, defined by

$$\mathrm{Nu} = \frac{hL}{k_l} \tag{12}$$

where

$$h = \frac{k_l}{\Delta T}\left|\frac{\partial T}{\partial x}\right|_{x=0,\,x=L} \tag{13}$$

In terms of nondimensional variables, the local Nusselt number can also be expressed at

$$\mathrm{Nu} = \left|\frac{\partial \theta}{\partial X}\right|_{X=0,\,X=1} \tag{14}$$

The average Nusselt number for a vertical wall is obtained by integrating the local Nusselt number in the Y-direction to yield, e.g., for $X = 0$

$$\overline{\mathrm{Nu}} = \frac{1}{A}\int_0^A \left|\frac{\partial \theta}{\partial X}\right|_{X=0} dY \tag{15}$$

The distributions of the local and average Nusselt number along the hot and cold walls for $\Delta T = T_h = 3.98$°C, 8°C, and 12°C are illustrated in Figures 5–7, respectively. The average Nusselt number across the cavity and at each sidewall is constant in all cases and increasing with Ra.

At small temperature difference (e.g., $\Delta T = 3.98$°C in Figure 5) it can be seen that the heat transfer rate reaches its maximum at the bottom of the cold wall and decreases in Y-direction as the fluid rises along the cold wall. At the hot wall the water descends, and the horizontal heat transfer decreases from top to bottom. This is valid for all Rayleigh numbers. The local heat transfer exhibits a remarkable symmetry with respect to the $Y = 0.5$ line.

At $\Delta T = 8$°C (Figure 6) the flow is upward at both sidewalls, and downflow is in the center. The horizontal heat transfer is highest at the bottom of the cavity and lowest at the top. For all Rayleigh numbers, two convective roll cells have approximately equal size (see Figure 3) because of the slight asymmetry of the density with respect to the vertical centerline. For the perfect symmetry case ($\Delta T = 7.96$°C), both curves of local Nusselt number at the cold and hot surfaces are identical.

At high temperature differences (Figure 7) the local heat transfer varies strongly with height. This dependence is different at both cold and hot sidewalls. Although the symmetry at low Ra is moderate, symmetry is broken at higher Rayleigh numbers. At $\mathrm{Ra} = 10^6$, because of the development of the vortex adjacent to the cold wall the local Nusselt number first decreases and then increases along the positive Y-axis; the crossing point is found at $Y = 0.40$.

Figure 8 shows the effects of Rayleigh number and temperature difference on average Nusselt number. All curves start at Nu = 1 when Ra is small. Then, increasing the Rayleigh number leads to an increase in Nusselt number for all ΔT cases. According to the value of the heat-transfer rate, two ranges of each curve can be identified: (1) At lower Rayleigh number, the average Nusselt number increases moderately with Ra. (2) As Ra continues to increase the slope of the curve soon gets larger and remains constant.

From Figure 8 it can be seen that for the monotonic density case ($\Delta T = 3.98$°C) with single convective roll cell the total heat transfer rate is highest. At $\Delta T = 8$°C, with one pair of counterrotating convective roll cells, the heat-transfer rate is

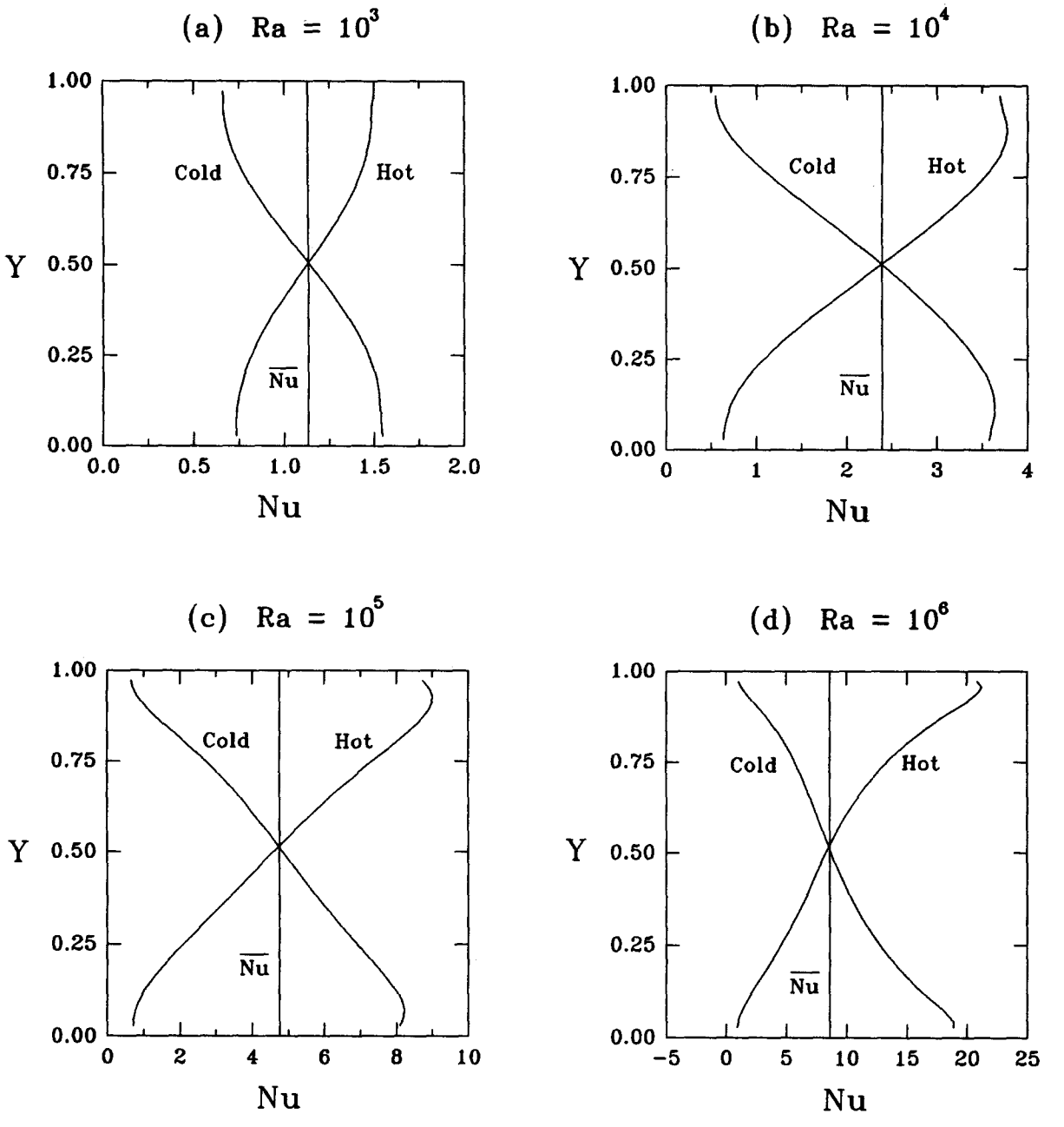

Figure 5 Distributions of local Nusselt number on hot and cold surfaces for ΔT = 3.98°C

minimized. The explicit minimum is reached at $\Delta T = 2T_0$ (7.96°C). As the temperature difference reaches 12°C, the curve shifts upward again as the effect of density inversion becomes weaker. This behavior substantiates results presented in the previous section. Furthermore, Figure 8 shows good agreement with Lin and Nansteel (1987).

In analyzing and modeling heat-transfer problems, it is most desirable to provide mean Nu(Ra) correlations. For the case of $A = 1.0$, two correlations can be derived as

$$\overline{\mathrm{Nu}} \simeq 1 \quad \mathrm{Ra} \lesssim 10^3 \tag{16}$$

$$\overline{\mathrm{Nu}} = C\,\mathrm{Ra}^m \quad 10^3 < \mathrm{Ra} < 10^6 \tag{17}$$

Unlike in convection problems without density inversion, the coefficient C is not a constant but a function of the temperature difference (cf. Table 4). This is because the position of the maximum density plane in the liquid varies directly with ΔT to influence the heat-transfer rate. These correlations are consistent with those of Lin and Nansteel (1987) for non-Boussinesq fluids ($m = 0.30$) and with those of Emery and Chu (1965) for Boussinesq fluids ($m = 0.25$).

Vertical velocity profile

Variations of vertical velocity at $Y = 0.5$ are analyzed. For the $\Delta T = 3.98$°C case, the velocity varies sinusoidally along $Y = 0.5$ line at lower Ra. Increasing Ra results in typical boundary layer flow at the side walls. The velocity profiles at $\Delta T = 8$°C reflect the symmetry of the flow pattern. With the density maximum closer to the cold wall (Figure 9) the velocity profile is nonsymmetric. The boundary layer flow is mainly developed near the hot wall. At highest Ra the flow in the core region is minimized, and boundary layer flow adjacent to the cold wall is established.

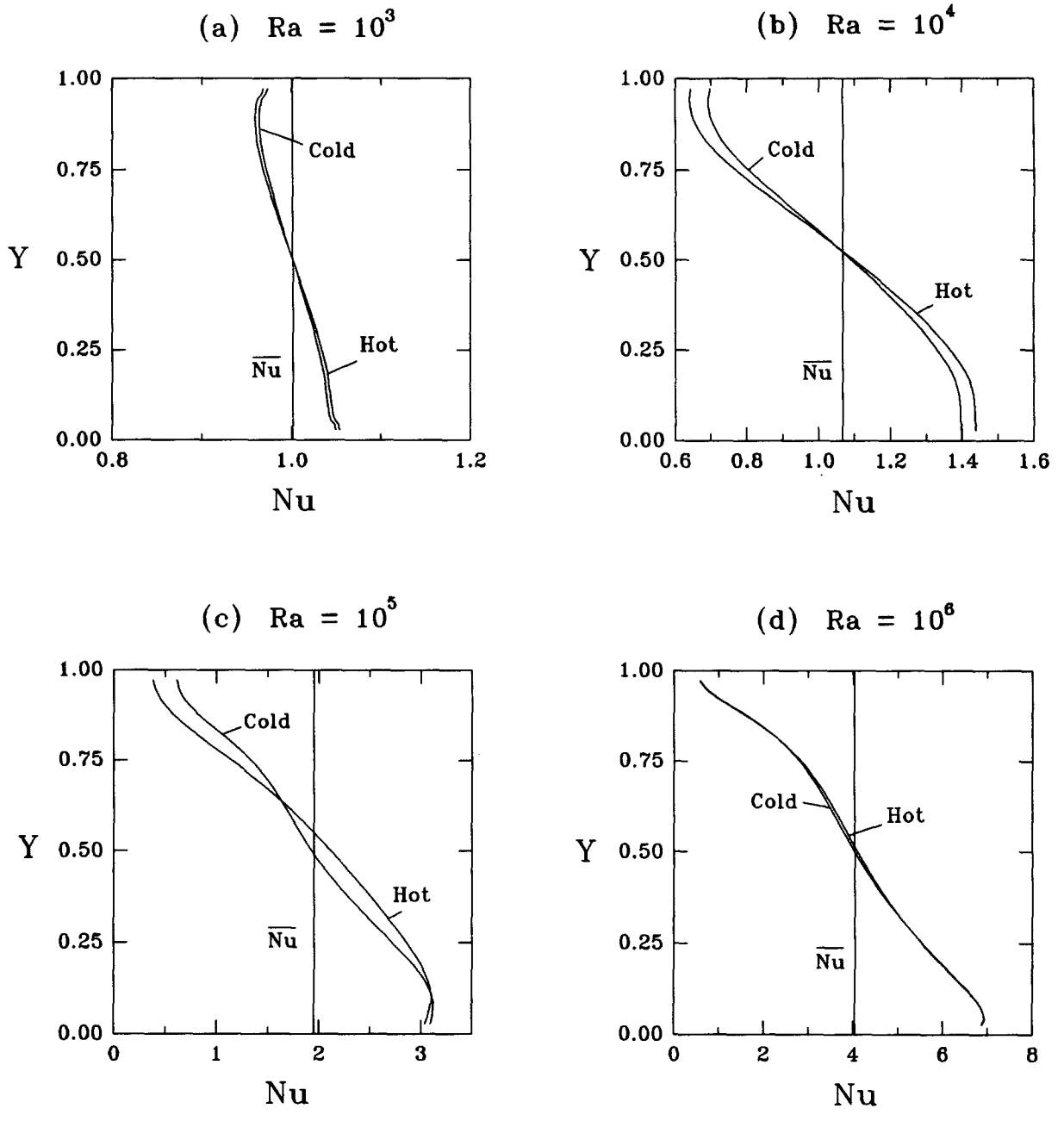

Figure 6 Distributions of local Nusselt number on hot and cold surfaces for $\Delta T = 8°C$

Aspect ratio effect

For buoyancy-induced flows in a confined cavity, a most important study is the effect of aspect ratio on convective flow characteristics. In the present study, computations have been carried out for $A = 2.0$, 1.0, 0.5, 0.25, and 0.125 with the width is held constant.

Numerical results for $\Delta T = 12°C$ and $Ra = 10^6$ are shown in Table 5. From that table it appears that the total heat transfer rate reaches a maximum value at $A = 1$. For $2 \geq A > 1$ the decrease results from the shear stress at the vertical walls, which retards the abrupt changes in the temperature and flow fields and in turn, reduces the temperature gradient at the side walls. For $A < 1$, the reduction in heat transfer is directly related to the reduction of H, which in turn is proportional to the effective buoyancy force. In the asymptotic case ($A \ll 1$) the dominant heat transfer mechanism is conduction. Figure 10 shows that the convective roll cell resulting from the density inversion is adjacent to the cold wall at small aspect ratios and confined to the lower corner of the cold wall at $A \geq 0.5$. In accordance with Seki et al. (1978) the heat transfer diminishes for increasing $A > 1$.

Conclusion

Numerical simulations have been carried out to study natural convection in a confined environment that includes density inversion. A non-Boussinesq parabolic density profile was included in the numerical FEM scheme. Numerical results obtained in the present study demonstrate the significant effect of density inversion on the heat-transfer and flow patterns in an enclosed cavity. It is found that the location of the

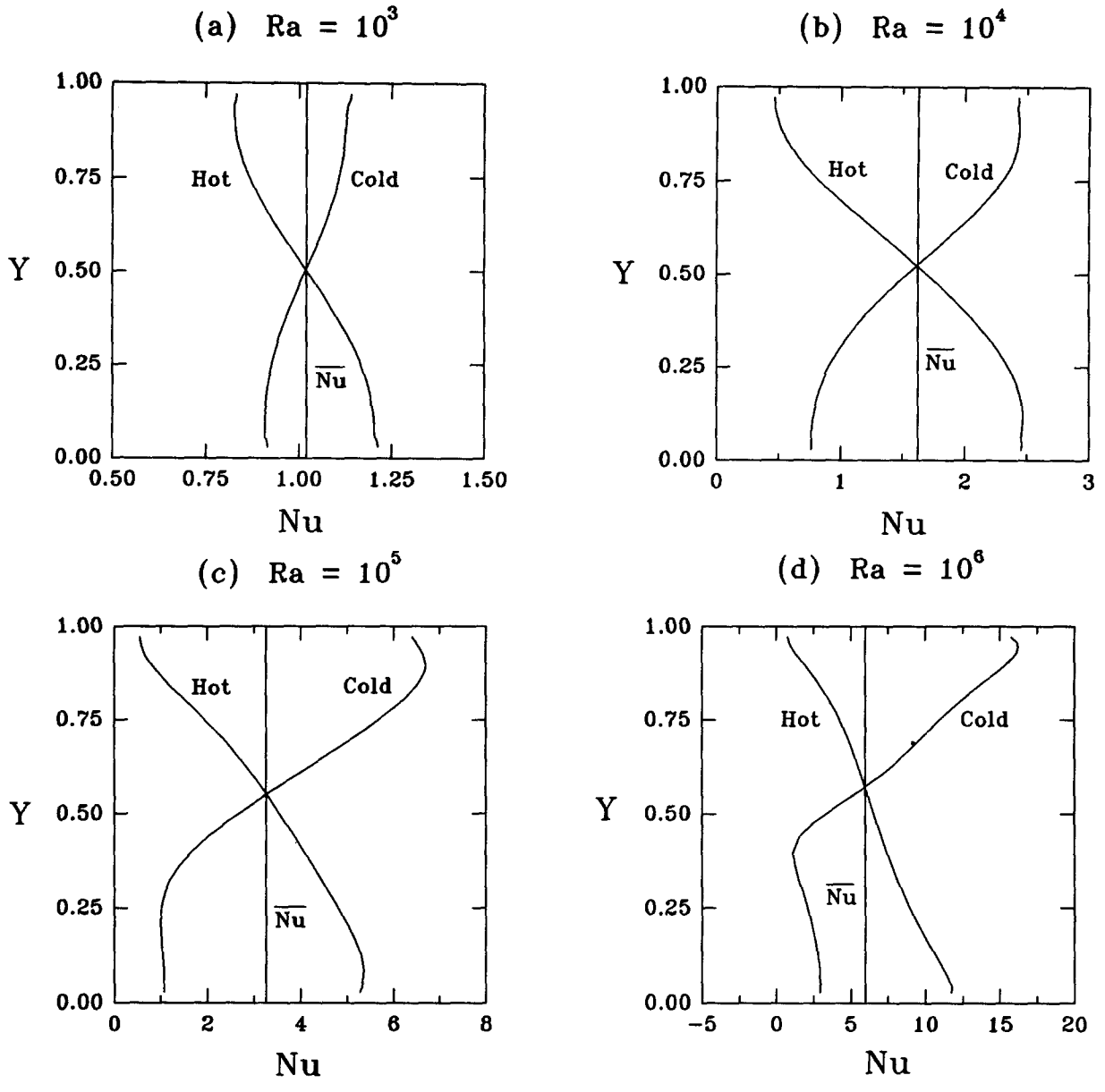

Figure 7 Distributions of local Nusselt number on hot and cold surfaces for $\Delta T = 12°C$

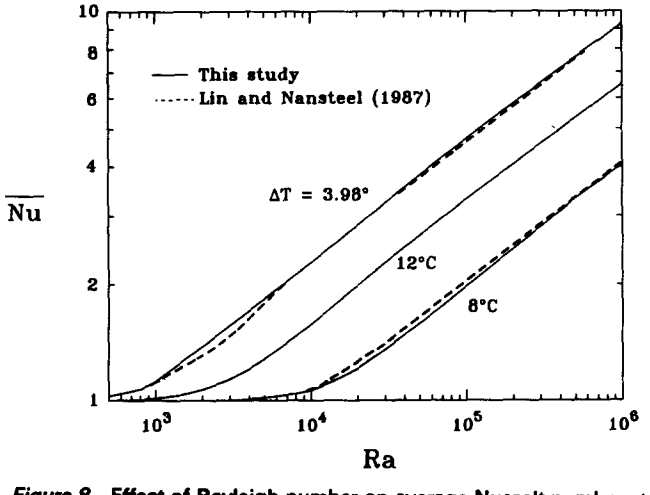

Figure 8 Effect of Rayleigh number on average Nusselt number at various ΔT values for $A = 1$

maximum density within cold water determines the flow character and alters the distribution of the local Nusselt number at vertical walls. With density inversion, a convective flow pattern develops at each side of the surface separated by the $\Psi = 0$ plane. Convective heat transfer is reduced because of the added resistance between the two counterrotating cells.

For a completely symmetric density profile case, the maximum density surface ($\theta = 0$) always coincides with the

Table 5 Numerical results for $\Delta T = 12°C$ and $Ra = 10^6$ at various aspect ratio values

A (H/L)	Grid	$\overline{Nu}$	Ψ_{max} ($\times 10^3$)	$\lvert\Psi_{min}\rvert$ ($\times 10^3$)
2	45 × 55	5.858	5.018	9.191
1	43 × 43	6.516	1.816	5.228
0.5	55 × 45	6.266	0.301	2.943
0.25	65 × 45	2.638	0.275	1.138
0.125	85 × 45	1.045	0.081	0.187

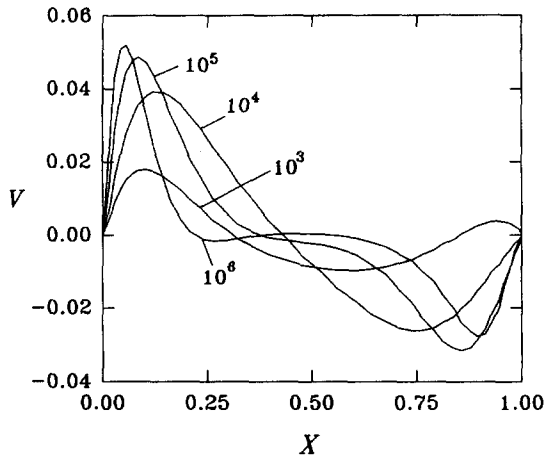

Figure 9 Variations of vertical velocity at Y = 0.5 for ΔT = 12°C under various Rayleigh numbers

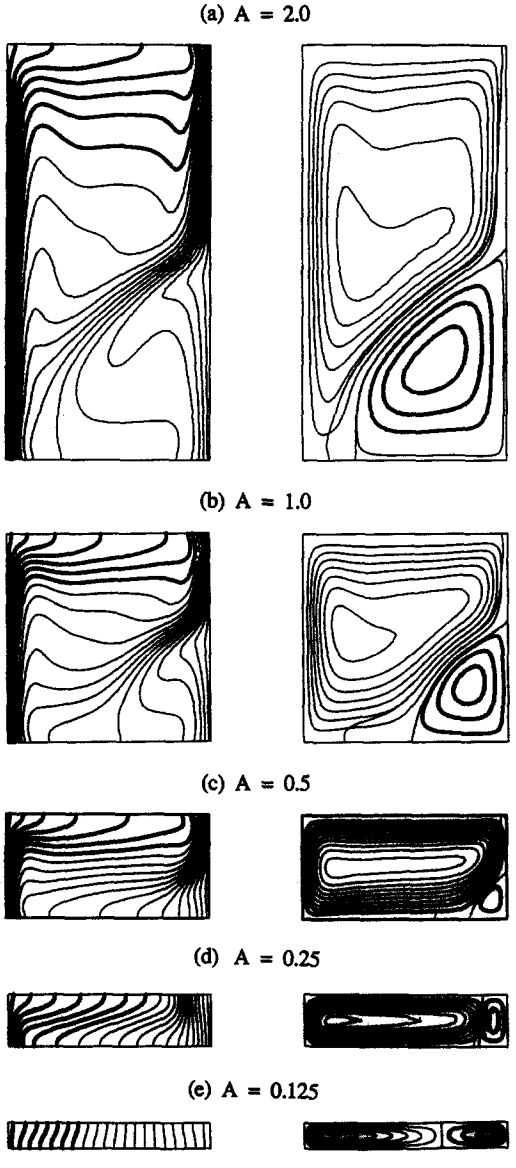

Figure 10. Effect of aspect ratio on the temperature field and convective flow pattern for ΔT = 12°C and Ra = 10^6

$\Psi = 0$ surface; no penetration of a convection cell across the density inversion surface is observed. As soon as the density profile symmetry is broken the flow becomes penetrative, and one vortex expands at the expense of the other. The velocity profile reflects the asymmetry while the local Nusselt number changes in a complicated function in vertical direction. The aspect ratio study shows that the second roll may either occupy a corner of the cavity only in high-aspect ratio containers, or expand from bottom to top of the cavity in small-aspect ratio containers. The results suggest that the total heat transfer reaches its maximum at $A = 1$.

Acknowledgments

Funding for this work provided by NASA MSAD under grant NAG3-1094 is gratefully acknowledged.

References

Chandra, D. and Holland, L. R. 1983. Density of liquid $Hg_{1-x}Cd_xTe$. *J. Vac. Sci. Tech.*, **A1**, 1620–1624

de Vahl Davis, G. 1983. Natural convection on air in a square cavity—a bench mark numerical solution. *Int. J. Num. Meth. Fluids*, **3**, 249–264

Emery, A. and Chu, N. C. 1965. Heat transfer across vertical layers. *ASME J. Heat Transfer*, **87**, 110–116

FIDAP. 1990. *User's Manual.* Fluid Dynamics International, Inc., Evanston, IL

Lin, D. S. and Nansteel, M. W. 1987. Natural convection heat transfer in a square enclosure containing water near its density maximum. *Int. J. Heat Mass Transf.*, **30**, 2319–2329

Merker, G. P., Waas, P. and Grigull, U. 1973. Onset of convection in a horizontal water layer with maximum density effects. *Int. J. Heat Mass Trans.*, **22**, 505–515

Moore, D. R. and Weiss, N. O. 1973. Nonlinear penetrative convection. *J. Fluid Mech.*, **61**, 553–581

Musman, S. 1968. Penetrative convection. *J. Fluid Mech.*, **31**, 343–360

Robillard L. and Vasseur, P. 1981. Transient natural convection heat transfer of water with maximum density effect and supercooling. *ASME J. Heat Transfer*, **103**, 528–534

Seki, N., Fukusako, S. and Inaba, H. 1978. Free convective heat transfer with density inversion in a confined rectangular vessel. *Wärme- und Stoffübertragung*, **11**, 145–156

Sohn, J. L. 1988. Evaluation of FIDAP on some classical laminar and turbulent benchmarks. *Int. J. Num. Mech. in Fluids*, **8**, 1469–1490

Sun, Z. -S., Tien C. and Yen, Y. -C. 1969. Thermal instability of a horizontal layer of liquid with maximum density. *AIChE J.*, **15**, 910–915

Tien, C. 1968. Thermal instability of a horizontal layer of water near 4°C. *AIChE J.*, **14**, 652–653

Veronis G. 1963. Penetrative convection. *Astrophysical J.*, **137**, 641–663

Walden, R. W. and Ahlers, G. 1981. Non-Boussinesq and penetrative convection in cylindrical cell. *J. Fluid Mech.*, **109**, 89–114

Watson, A. 1972. The effect of the inversion temperature on the convection of water in an enclosed rectangular cavity. *Q. J. Mech. Appl. Math.*, **25**, 423–446

Appendix:

Conversion of results between the systems using different length scales

In natural convection in a cavity with two differentially heated vertical walls, the cavity width in the direction of the temperature gradient is often considered the characteristic length when normalizing the governing equations. However, often the cavity height is chosen as the length scale as heating

occurs at the vertical wall. To compare results from the literature that are based on different length scales, it is highly desirable to find relations between these two similarity definitions.

With H as characteristic length, Rayleigh number and Nusselt number are defined as

$$Ra_H \equiv \frac{g\gamma(\Delta T)^2 H^3}{\alpha\nu} \tag{18}$$

$$\mathrm{Nu}_H \equiv \frac{hH}{k_1} \tag{19}$$

Thus, the dimensionless average Nusselt number across $X = 0$ becomes

$$\overline{\mathrm{Nu}}_H = \int_0^1 \left|\frac{\partial\theta}{\partial X}\right|_{X=0} dY \tag{20}$$

and the dimensionless stream function is expressed as

$$\Psi_H = \int_0^1 \mathrm{U}\, dY \tag{21}$$

Comparing the above equations with corresponding equations in this study, four relations are found:

$$\mathrm{Ra}_H = A^3 \mathrm{Ra}_L \tag{22}$$

$$\overline{\mathrm{Nu}}_H = A\overline{\mathrm{Nu}}_L \tag{23}$$

$$\mathrm{U}_H = A^{-1/2}\mathrm{U}_L \tag{24}$$

$$\Psi_H = A^{-3/2}\Psi_L \tag{25}$$

where $A = H/L$. These equations have been applied in this study to compare with other authors' results.